


Internal-Flow-Mediated, Tunable One-dimensional Cassie-to-Wenzel Wetting Transition on Superhydrophobic Microcavity Surfaces during Evaporation

Prashant Pendyala, Hong Nam Kim, Harpreet S. Grewal, Uikyu Chae, Sungwook Yang, Il-Joo Cho, Simon Song & Eui-Sung Yoon


To cite this article: Prashant Pendyala, Hong Nam Kim, Harpreet S. Grewal, Uikyu Chae, Sungwook Yang, Il-Joo Cho, Simon Song & Eui-Sung Yoon (2019) Internal-Flow-Mediated, Tunable One-dimensional Cassie-to-Wenzel Wetting Transition on Superhydrophobic Microcavity Surfaces during Evaporation, *Nanoscale and Microscale Thermophysical Engineering*, 23:4, 275-288, DOI: [10.1080/15567265.2019.1660439](https://doi.org/10.1080/15567265.2019.1660439)

To link to this article: <https://doi.org/10.1080/15567265.2019.1660439>

 View supplementary material [↗](#)

 Published online: 30 Aug 2019.

 Submit your article to this journal [↗](#)

 Article views: 240

 View related articles [↗](#)

 View Crossmark data [↗](#)

 Citing articles: 1 View citing articles [↗](#)



Internal-Flow-Mediated, Tunable One-dimensional Cassie-to-Wenzel Wetting Transition on Superhydrophobic Microcavity Surfaces during Evaporation

Prashant Pendyala^{a,b,*}, Hong Nam Kim^{id a,c,*}, Harpreet S. Grewal^d, Uikyu Chae^{a,e},
Sungwook Yang^f, Il-Joo Cho^{a,c}, Simon Song^{b,g}, and Eui-Sung Yoon^{id a,h}

^aCenter for BioMicrosystems, Korea Institute of Science and Technology, Seoul, Republic of Korea; ^bInstitute of Nano Science and Technology, Hanyang University, Seoul, Republic of Korea; ^cDivision of Bio-Medical Science and Technology, KIST School, Korea University of Science and Technology, Seoul, Republic of Korea; ^dDepartment of Mechanical Engineering, School of Engineering, Shiv Nadar University, India; ^eSchool of Electrical Engineering, Korea University, Seoul, Republic of Korea; ^fCenter for Intelligent & Interactive Robotics, Korea Institute of Science and Technology, Seoul, Republic of Korea; ^gDepartment of Mechanical Engineering, Hanyang University, Seoul, Republic of Korea; ^hDivision of Nano & Information Technology, KIST School, Korea University of Science and Technology, Seoul, Republic of Korea

ABSTRACT

Superhydrophobic textured surfaces are known to maintain a nonwetted state unless external stimuli are applied since they can withstand high wetting pressure. Herein, we report a new category of tunable, one-dimensional (1D) Cassie-to-Wenzel wetting transitions during evaporation, even on superhydrophobic surfaces. The transition initiates at the periphery of the evaporating drop, and the wetting transition propagates toward the center of the drop. The transitions are observed for surfaces with wetting pressures as high as $\sim 7,568$ Pa, which is much higher than the Laplace pressure, i.e., ~ 200 Pa. In situ high-contrast fluorescence microscopy images of the evaporating drop show that the transition is induced by preferential depinning of the air-water interface and subsequent formation of air bubbles in the cavities near the three-phase contact line. The evaporation-induced internal flow enhances the pressure within the water droplet and subsequently causes a Cassie-to-Wenzel wetting transition.

ARTICLE HISTORY

Received 12 March 2019
Accepted 20 August 2019

KEYWORDS

1D wetting transition; Cassie state; Wenzel state; internal flow; evaporation


Introduction

Conservation and manipulation of water drops on superhydrophobic surfaces are important for both biological and physical phenomena, including mass [1–6] and heat transfer [7–10]. Superhydrophobic surfaces typically exhibit high wetting pressures. A droplet deposited on these surfaces rests on top of the surface elements with air trapped underneath. This heterogeneous wetting regime is known as a ‘Cassie state’. On the other hand, if the droplet fills the surface elements, it exhibits a homogeneous wetting regime known as a ‘Wenzel state’. The transition from the Cassie state to Wenzel state occurs when the drop experiences a threshold effective pressure [11] (wetting pressure) either due to excessive Laplace pressure or external stimuli such as pressure [12, 13], vibration [14], voltage [15], or droplet bouncing [16]. Furthermore, the air trapped below the drop acts as an ancillary factor in the wetting transition [17]. On open cavity surfaces with protruding structures, such as pillars, a drop in the Cassie

CONTACT Eui-Sung Yoon  esyoon@kist.re.kr  Center for BioMicrosystems, Korea Institute of Science and Technology, Seoul 02792, Republic of Korea; Simon Song  simonsong@hanyang.ac.kr  Institute of Nano Science and Technology, Hanyang University, Seoul 04763, Republic of Korea

*These authors contributed equally to this work

Color versions of one or more of the figures in the article can be found online at www.tandfonline.com/umte.

 Supplemental data for this article can be accessed [here](#).

state traps air as a continuous layer, and the length of this layer is large relative to the structure dimensions [17]. On closed cavity surfaces, air is completely confined within the structures [17], and these structures are expected to have a greater resistance to the Cassie-to-Wenzel transition than the protruding structures [15, 17, 18].

The wetting transition is mediated by the following mechanisms [11, 19] (Figure S1): (i) the contact line at the edge of the interstices vertically propagating as the local contact angle (θ^*) exceeds the equilibrium contact angle (θ_e) [20], called as ‘depinning transition’ and (ii) the sag of the air-water interface reaching the bottom of the cavity, called as ‘sag transition’ [21]. On engineered surfaces, the expected sag of the air-water interface is usually small relative to the cavity depth, and thus, depinning is the main transition mechanism. A useful criterion for depinning transitions can be obtained by considering the surface energy barrier between the Cassie and Wenzel states [11]. For square-shaped, closed microcavity surfaces, the wetting transition occurs when the work performed by the effective pressure (ΔP) within the drop ($W_p \sim \Delta P a^2 H$) is greater than the surface energy barrier of the Cassie-to-Wenzel transition ($4aH\sigma_{lg} \cos\theta_e$). Hence, we obtain the following pressure criterion for the depinning wetting transition of microcavity surfaces:

$$\Delta P_{depin} > \frac{-4\sigma_{lg} \cos\theta_e}{a} \quad (1)$$

where σ_{lg} is the surface tension of water, a is the width and H is the depth of the cavity structures, and θ_e is the equilibrium contact angle. Similarly sag transition occurs when the sag (S) of the air-water interface contacts with the bottom of the cavity (Figure S1). The criteria of sag transition is given by

$$\Delta P_{sag} > \frac{2\sigma_{lg}}{\left(\frac{a^2}{8H} + \frac{H}{2}\right)} \quad (2)$$

When a wetting transition occurs via external stimuli, previous studies have consistently shown that the wetting transition is instantaneous and uniform across the base of the drop [22]. However, recently, Bormashenko *et al.* [23, 24], reported that a drop on a polymeric porous substrate is subject to external vibration, and the Cassie-to-Wenzel transition is initiated near the contact line. Such a transition phenomenon is termed a one-dimensional (1D) wetting transition. A similar 1D wetting transition of a drop was also reported in electrowetting experiments [15]. These studies indicate that the wetting transition is not always uniform at the drop-surface interface and suggest the existence of other mechanisms for the 1D wetting transition.

Evaporation of a water drop is mediated by differential mass transfer regime over the drop surface which induces vigorous flows inside the drop. Role of such evaporation-induced internal flows on wettability of the drop was neglected previously. However, it was shown that flow inside an evaporating drop exhibits spatio-temporally varying pressures which are up to an order of magnitude larger than the typical Laplace pressure values. The understanding on the evaporation-induced pressure gradients is potentially useful to tune the wetting characteristics on superhydrophobic surfaces. In this work, we demonstrate a new directional wetting transition category based on the internal flow dynamics of an evaporating drop using engineered microcavity structures. For this purpose, we monitored the time-dependent characteristics of evaporating drops on carefully designed microcavity surfaces under a large range of wetting pressures (250–30,000 Pa). We related the nature of the evaporative flux over the surface of these drops to the spatiotemporal variation in the wetting state. The mechanisms of the wetting transitions at the individual cavity level and drop level were studied using *in situ* fluorescence microscopy.

Experimental details

Fabrication of microcavity patterns

Microcavity patterns were fabricated on Si (100) wafers using photolithography and reactive ion etching (RIE) techniques. In total, eight cavity surfaces were generated with varying cavity sizes but constant solid

wall thickness of $2\ \mu\text{m}$ (Figure 1(a)). A schematic of the detailed fabrication procedure is shown in Figure S2(a). The roughness of the solid connected region of the patterns and the reference flat samples used for the study was negligible relative to the dimensions of the cavity structures (Figure S2(b)). A plasma-enhanced chemical vapor deposition technique was used to deposit thin layers (approximately 20 nm) of fluorinated diamond-like carbon (FDLC) coatings. A polytetrafluoroethylene (PTFE) coating (approximately 20 nm) was obtained using plasma enhanced chemical vapor deposition (PECVD) as the first stage of the BOSCH process.

Observation of wetting transition

The equilibrium static contact angles of the FDLC-coated and PTFE-coated flat surfaces were measured using the sessile drop method to be approximately 92° and 108° , respectively. To determine the wetting characteristics of the surfaces, a water droplet was allowed to evaporate on the microcavity surfaces, and side-view and top-view images were obtained using a bright-field optical microscope. Changes in the wetting characteristics were primarily determined based on changes in the optical contrast of the top-view images. Side-view imaging was used to determine the drop shape characteristics over the evaporation time, particularly at the time of the wetting transition. For all the evaporation experiments, a drop volume of $3\ \mu\text{L}$ was used. The temperature and relative humidity (RH) were maintained at $24 \pm 1^\circ\text{C}$ and $45 \pm 5\%$, respectively.

In situ fluorescence imaging

In situ fluorescence microscopy experiments were performed using a Zeiss Axioplan 2 Upright fluorescence microscope. For visualization, a $10\ \mu\text{M}$ fluorescein sodium salt (Sigma-Aldrich) solution in deionized water was prepared.

Results and discussion

1D wetting transition during water drop evaporation

We fabricated square microcavity structures with critical dimensions from 2 to $40\ \mu\text{m}$ and a depth of $1\ \mu\text{m}$ (Figure 1 and Table 1). The surface energy of the microcavities was controlled by coating them with polytetrafluoroethylene (PTFE) and fluorinated diamond-like carbon (FDLC). The PTFE coating on the microcavities resulted in superhydrophobicity, while the FDLC coating induced hydrophobicity. The specifications of the microcavity structures and chemical coatings on them were chosen such that the water affinity of the experimental surfaces is varied from barely hydrophobic to superhydrophobic. Table 1

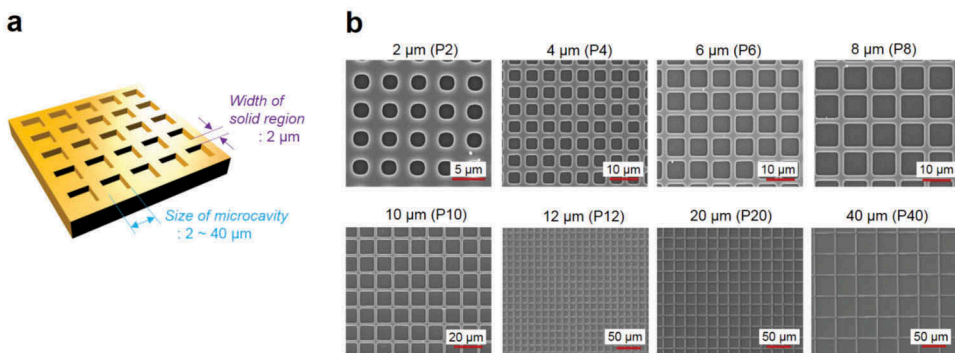


Figure 1. (a) Schematic illustration of a microcavity array. In this study, only the size of the microcavity was varied, while the width of the solid region between the cavity structures and the depth were maintained at $2\ \mu\text{m}$ and $1\ \mu\text{m}$, respectively. (b) Scanning electron microscopy images of the fabricated microcavity surfaces.



Table 1. Geometrical characteristics of the microcavity patterns along with the corresponding experimental contact angle, depinning wetting pressure (Equation 1), and sag wetting pressures (Equation 2). Wetting transition characteristics of each microcavity surface are also indicated. The width of the solid area between the cavity structures is around $2\ \mu\text{m}$ as shown in Figure 1(a). The pressure criteria for wetting (wetting pressure) for each of the cavity surface, based on ΔP_{depin} and ΔP_{sag} values, is highlighted in blue.

Sample	Static contact angle (degrees)			ΔP_{depin} (Pa)		ΔP_{sag} (Pa)		1D transition (Yes/No)	
	FDLC	PTFE	FDLC & PTFE	FDLC	PTFE	FDLC & PTFE	FDLC & PTFE	FDLC	PTFE
Flat	92.16 ± 0.66	108.13 ± 0.48	Not applicable	Not applicable	Not applicable	Not applicable	Not applicable	Not applicable	Not applicable
2 (P2)	103.37 ± 1.53	119.34 ± 0.32	5,081	30,272	1,44,000	Yes	Yes	Yes	No
4 (P4)	113.82 ± 1.57	129.57 ± 1.26	2,540	15,136	57,600	Yes	57,600	Yes	No
6 (P6)	118.43 ± 0.69	131.52 ± 2.21	1,693	10,091	28,800	Yes	28,800	Yes	No
8 (P8)	121.26 ± 0.49	133.77 ± 0.56	1,270	7,568	16,941	Yes	16,941	Yes	Yes
10 (P10)	124.30 ± 0.37	140.85 ± 0.03	1,016	6,054	11,077	Yes	11,077	Yes	Yes
12 (P12)	126.45 ± 1.86	141.75 ± 0.84	846	5,045	7,783	Yes	7,783	Yes	Yes
20 (P20)	126.85 ± 3.59	145.20 ± 1.42	508	3,027	2,851	Yes	2,851	Yes	Yes
40 (P40)	143.61 ± 1.58	151.99 ± 1.13	254	1,513	718	Not applicable	718	Not applicable	Not applicable

shows the equilibrium contact angles of the microcavity patterns along with the corresponding depinning and sag wetting transition pressures obtained using Equation 1 and 2 respectively.

The depinning pressure (ΔP_{depin}) and sag pressures (ΔP_{sag}) for the patterned surfaces were much larger than the typical Laplace pressure values. Ideally, such surfaces are not expected to show any wetting transitions unless external force or pressure is applied. Furthermore, the dominant mechanism of wetting transition depends on the magnitudes of ΔP_{depin} and ΔP_{sag} for the corresponding surfaces. For all the FDLC-coated surfaces, $\Delta P_{depin} < \Delta P_{sag}$ (Table 1). Whereas, for PTFE-coated surfaces, $\Delta P_{depin} < \Delta P_{sag}$ when microcavities were smaller than $20\ \mu\text{m}$. For PTFE-coated P20 and P40 surfaces, $\Delta P_{depin} > \Delta P_{sag}$. That is, except for PTFE-coated P20 and P40 surfaces, for all the remaining surfaces depinning of the air-water interface at the sidewall of the cavity is believed to be a main reason for the wetting transition (Figure S1). By comparing the magnitudes of ΔP_{depin} and ΔP_{sag} for each of the surface, the threshold pressure at which cavities on them are expected to exhibit wetting transition is clearly indicated in Table 1. From here on, this threshold pressure for wetting transition is referred to as ‘wetting pressure’ of the corresponding surface.

As expected, the drops deposited on the microcavity surfaces were initially in the Cassie state and did not show a wetting transition. However, when the drop was allowed to evaporate, wetting transitions were observed at the end of the evaporation process on the surfaces with wetting pressures up to 7,568 Pa. Figure 2 shows representative images of the water droplets that exhibited wetting transitions and those that did not exhibit wetting transitions at the end of the evaporation process. We found that both the size of the microcavity and the surface energy affect the wetting transition during the evaporation of a water droplet. As shown in Table 1, on the FDLC-coated microcavity surfaces, all water droplets exhibited a wetting transition, whereas on the PTFE-coated substrate surfaces, the water droplets only showed a transition when the microcavities were larger than $6\ \mu\text{m}$ (Figures 2 and S3). The PTFE-coated P2, P4, and P6 surfaces with very large wetting pressures of 30,272 Pa, 15,136 Pa, and 10,091 Pa, respectively, showed no wetting transitions (Table 1). These results show that a water drop does not experience a Cassie-to-Wenzel wetting transition during the evaporation process when the

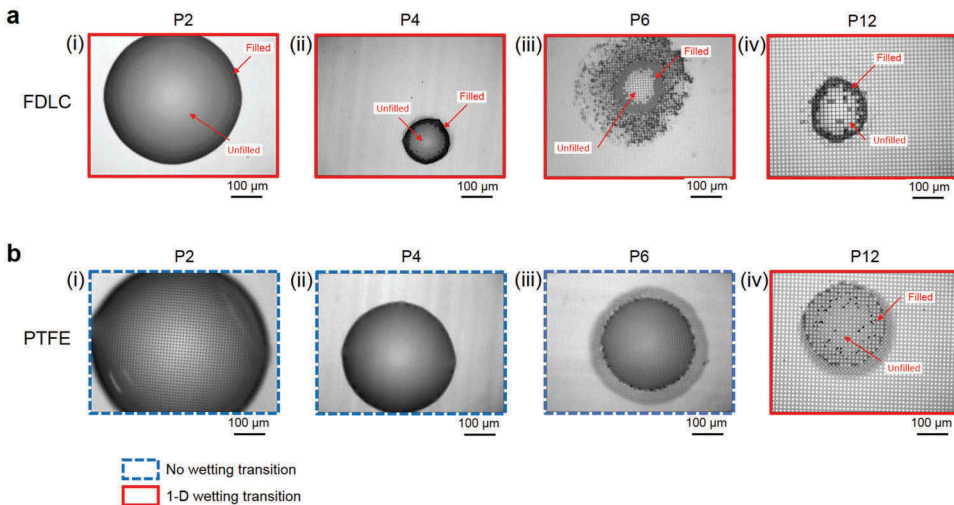


Figure 2. Representative optical microscope images of a water droplet at the end of the evaporation process. (a) FDLC surfaces. (b) PTFE surfaces. The images highlighted by a red solid line are of the evaporation of a water drop exhibiting a 1D wetting transition. In these cases, the wetting transition begins at the periphery of a water drop and propagates toward its center. The images highlighted in the dashed blue lines are of evaporation of a water droplet without a wetting transition. See the Supplementary material for the time-lapse videos showing wetting characteristics of a(i) and b(i) respectively.

drop is on sufficiently small microcavities with low surface energy, implying small feature size and low surface energy have synergistic roles in long-term wetting stability.

To demonstrate the time-dependent evolution of the wetting transition, we conducted a live-imaging experiment from the droplet deposition until the evaporation process was complete. Figure 3 shows the time-lapse images of evaporating drop on FDLC-coated and PTFE-coated P6 surfaces. FDLC-coated P6 surface exhibited significant optical contrast at the cavities showing that the cavities are impaled due to the wetting transition. It can be seen that the wetting transition on FDLC-coated P6 was not homogeneous and random, but directional. The transition began at the periphery of the drop and propagated toward the center. On the other hand, the PTFE-coated P6 surface did not exhibit any change in optical contrast showing that cavities are not impaled during the evaporation. In this case, evaporation residue surrounding the three-phase contact line of the drop presented the only significant optical contrast. In the case of microcavities having feature size larger than 6 μm , once the wetting transition initiated, the transition phenomenon on FDLC-coated and PTFE-coated surfaces showed no significant differences in terms of its initiation and propagation. Because the wetting transition progressed from the periphery to the center in the r -direction, this phenomenon during evaporation is called the ‘1D wetting transition’.

At the onset of transition, the ratio of the microcavity size (a) to the radius of the water droplet at that time (r_t) was in the range of 0.04–0.2 (Figure S5). It can be observed that when a/r_t is small ($\ll 0.1$), the 1D transition was symmetric and uniform (Figure S3). Whereas, when a/r_t was large (>0.1), the transition was asymmetric and non-uniform. This may be because, when the drop radius at the time of 1D transition especially for larger cavity surfaces is on the order of the cavity size, the drop shape and tortuousness of its three-phase contact line are highly influenced by pinning ability of the cavity edges. Furthermore, the local physicochemical changes inside the drop may also be critically influenced by the individual cavity structures (Figure S3).

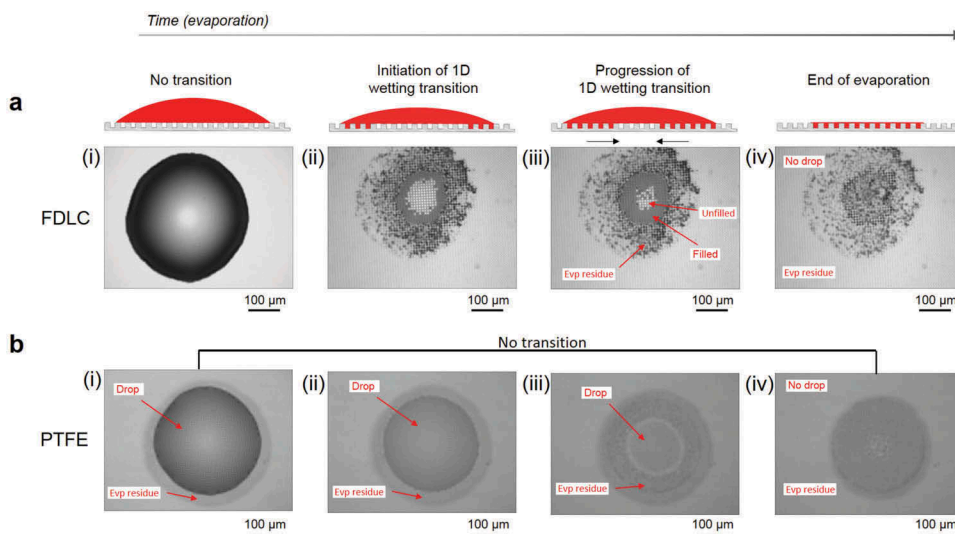


Figure 3. Time-lapse optical microscopy images of an evaporating water drop on a (a) FDLC-coated P6 surface and (b) PTFE-coated P6 surface. At a certain time point toward the end of the evaporation process, the FDLC surface exhibited a Cassie-to-Wenzel wetting transition at the periphery of the droplet (see a(ii)) that propagated toward the center (see a(iii)), showing 1D progression in the r -direction. The PTFE-coated P6 surfaces did not exhibit a wetting transition. See the Supplementary material for the corresponding time-lapse videos.

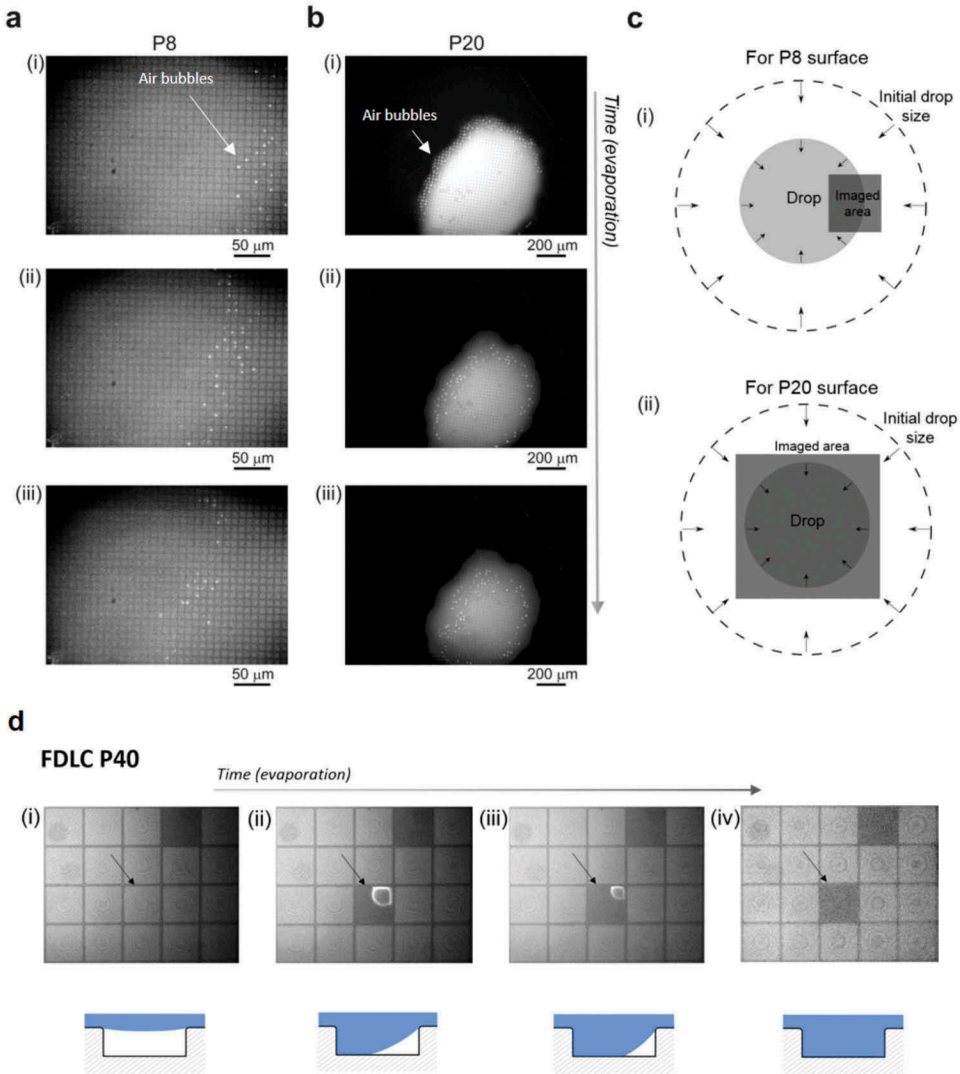


Figure 4. (a) Time-lapse fluorescence microscopy images of an evaporating drop on the FDLC-coated P8 surface. (b) Time-lapse fluorescence microscopy images of evaporating drops on FDLC-coated P20 surfaces. (c) Schematics showing the imaged areas of the drops shown in a(i)-a(iii) and b(i)-b(iii). (d) Time-lapse fluorescence microscopy images showing the filling of a cavity on the FDLC-coated P40 surface. a(i)-a(iii) show how the transition region moves from the region near the contact line (right-hand side) to the center for the drop (left-hand side). b(i)-b(iii) show how the transition region moves from near the contact line to the center of the drop. d(i)-d(iii) show the stages of the cavity (highlighted using an arrow) undergoing a transition. As shown in the corresponding schematics, the air-water interface at the cavity depins, leading to liquid filling the cavity. The air displaced from the cavity forms a bubble. The images show that the air bubble was stuck to the edges of the cavity and dissolved over time. See the Supplementary material for the corresponding time-lapse videos of a(i)-a(iii) and b(i)-b(iii) respectively.

Mechanism of the 1D wetting transition

In situ fluorescence microscopy

To monitor the filling of individual microcavities, we conducted *in situ* evaporation experiments using high-contrast fluorescence microscopy (Figure 4). This fluorescence imaging technique contributed to clarification of the 1D wetting transition mechanism. To visualize the dynamics within a water drop, we added fluorescein sodium salt (concentration of 10 μM) to deionized water. In the fluorescence microscopy experiments, we detected small, flash-like bright spots around the three-

phase contact line. These bright spots are due to enhanced contrast of the fluorescence signals at the surface of air bubbles [25, 26]. As the three-phase contact line moved due to evaporation, new bright spots appeared in advance of the receding three-phase contact line. As shown in Figure 4(d), a detailed analysis of the experiments on surfaces with large cavities showed that the bright spots represent air bubbles that form due to depinning of the air-water interface and subsequent filling of individual cavities.

To detect tiny air bubbles, fluorescence microscopy experiments on surfaces with smaller cavities (P8) were performed at higher magnification, and only a small portion of the drop was imaged (Figure 4(a,c(i))). On surfaces with larger cavities (P20), the air bubbles were large, and therefore, the air bubbles in the entire water drop could be imaged at lower magnification (Figure 4(b,c(ii))). Figure 4 shows the time-lapse fluorescence images of the evaporating drops on the FDLC-coated P8 and P20 surfaces. On the P8 surface, a sequential emergence of air bubbles from the periphery to the center of the water drop was visible over time. On the P20 surface, air bubbles were visible in a peripheral, ring-like pattern along the three-phase contact line. Similarly, new air bubbles formed around the periphery as the three-phase contact line receded due to evaporation.

The fluorescence and bright-field microscopy experimental results prove that the 1D wetting transitions occur due to preferential depinning of the air-water interface in the cavities near the three-phase contact line. According to Equation 1 and 2, the transition only occurs when the effective pressure above the microcavity is higher than the wetting pressure of the cavities. Hence, for 1D transition to occur, at some time point during evaporation, the pressure in the peripheral regions of the drop should become larger than the wetting pressure of the cavities. Furthermore, since the transition gradually progressed toward the center of the drop, the pressure distribution should be spatially and temporally varying. During evaporation, the mass flow within a drop is the most important temporally and spatially varying parameter. In the following section, we show that the evaporative mass transfer-induced internal flow within a water drop is responsible for the spatio-temporally varying pressure distribution which causes 1D wetting transition.

Evaporative flux and internal flow characteristics

The evaporative mass flux (J) from a sessile drop with a spherical cap is not uniform [27], and the flux (J) depends on the various physico-chemical characteristics of the drop and the surface. If the steady-state vapor concentration is ϕ at the surface of a drop (Figure 5), evaporation can be described by the steady-state diffusion equation $\nabla^2 \phi = 0$ [27]. The derivative of this equation at the surface gives the evaporative flux $J = -D\nabla\phi$, where D is the diffusivity of the vapor in air. Assuming the shape of a spherical cap and a sharp wedge-shaped boundary, the evaporative flux (J) scales as [28]

$$J \sim \bar{\rho}^{\beta-1} \quad (3)$$

where $\beta = \pi/2\pi - 2\theta$, $\bar{\rho} = \rho/r$, θ is the contact angle, and r is the drop radius (see Figure 5). That is, when $\theta > 90^\circ$ and $\beta > 1$, the evaporation rate near the top of the surface is high, while the evaporation rate near the contact line is larger when $\theta < 90^\circ$. The nonuniform evaporative flux along the drop surface and the contact line dynamics determine the characteristic internal flow inside a drop.

Furthermore, since the drop-surface area continuously decreases with the evaporation time and the evaporation rate is constant (Figure 5(c)), the same liquid volume must be transported through a decreasing area based on simple mass balance considerations [29]. Since the evaporative flux near the contact line is large, a radially diverging flow is generated over time, irrespective of the pinning characteristics of the contact line (Figure 5(a)) [29, 30].

Gelderblom *et al.* [28], described the internal flow characteristics in an evaporating drop with a pinned contact line as having a diverging flux, as shown in Equation 4. For their analysis, they modeled the liquid-substrate interface using a no-slip boundary condition. They showed that below a critical angle θ_c less than $\sim 133.4^\circ$, the evaporative flux determines the fluid flow near the contact line, and the velocity (U_f) and pressure (P_f) scale as [28]

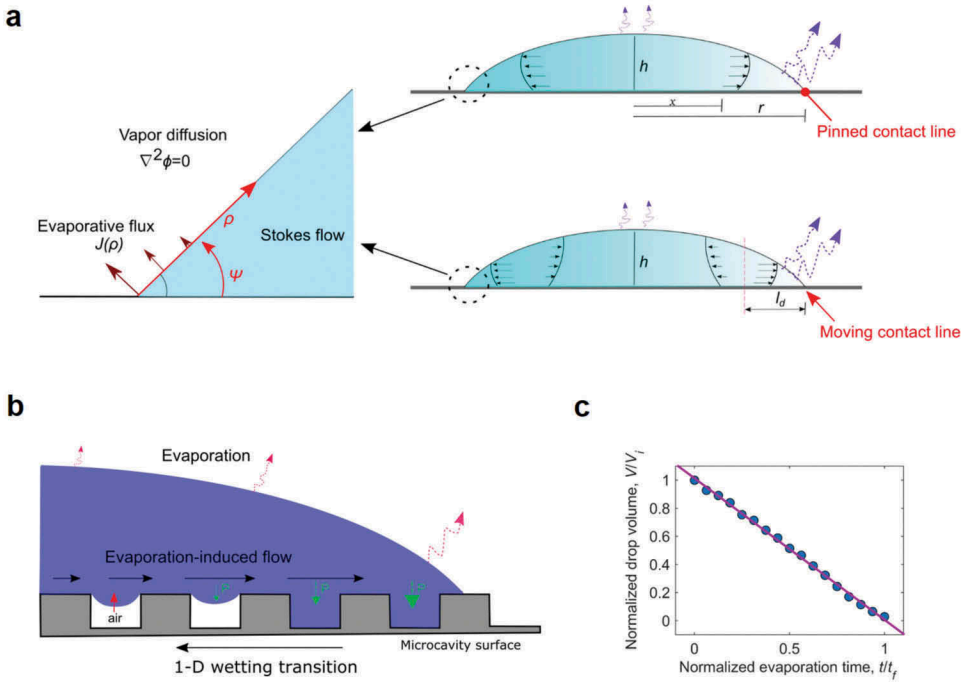


Figure 5. (a) The evaporative flux at the air-water interface. Irrespective of the contact line pinning, the evaporation flux is larger near the contact line. (b) Schematic illustrating the internal flow-induced wetting transition phenomenon near the three-phase contact line. (c) Change in the normalized volume of a water droplet in response to the normalized evaporation time. The volume of the water droplet deposited on the P6 surface decreases linearly upon evaporation.

$$U_f \sim \frac{1}{\theta(t)} G \bar{\rho}^{\beta-1} \quad (4)$$

$$P_f \sim \frac{1}{\theta(t)} \left(\frac{\eta G}{R(t)} \right) \bar{\rho}^{\beta-1} \quad (5)$$

where $G = D_{va} \Delta c / r \rho_l$ in which D_{va} is the diffusion constant for vapor in air, Δc is the vapor concentration difference between the surface of the drop and its surroundings, and ρ_l is the liquid density. A diverging evaporative flux gives rise to spatially diverging pressures and velocity fields near the contact line.

However, a freely moving three-phase contact line will lead to an additional velocity field with a mean flow directed away from the contact line [31]. As shown by Gelderblom *et al.* [28], the velocity solution for the moving contact line problem could be superimposed on the evaporation-driven solution mentioned above. However, the velocity field due to evaporation dominates near the contact line since velocity diverges at that point for $\theta < 90^\circ$. A crossover length [28, 31] at which the flux solution vanishes is shown to be at a distance l_d from the contact line, which is given by [30, 31]

$$l_d \sim \left(\frac{G \sqrt{R}}{V \theta} \right)^2 \quad (6)$$

where V is the velocity of the moving contact line. When the velocity of the moving contact line is on the order of $10 \mu\text{m/s}$, l_d is on the order of $100 \mu\text{m}$. Hence, at the time of the 1D transition, the flux

solution dominates for all our experimental cases. Therefore, a general expression for the effective pressure near the cavity can be written as

$$P_{eff}(\theta(t), r(t), x) = P_f(\theta(t), r(t), x) + \frac{2\gamma}{R(t)} + \rho_liquid g h \quad (7)$$

where R is the curvature radius of the drop, γ is the surface tension of the liquid, and g is the acceleration due to gravity. In the above equation, P_f is the pressure due to evaporation-induced internal flow, and the remaining two terms are due to the Laplace pressure (P_γ) and gravity, respectively. For a water drop with a very small contact angle ($\beta \sim 0.5$ – 0.6) and $G = 10^{-6}$ m/s, $\eta = 10^{-3}$ Pa s, and $R = 10^{-3}$ – 10^{-4} m, the pressure due to the internal flow, very close to the contact line ($\rho = 10^{-9}$ m), scales as $P_f \sim 10^3/\theta$, which is large compared to the Laplace pressure (~ 100 – 200 Pa).

Calculation of effective pressure over the course of water droplet evaporation

The magnitudes of P_γ and P_f (calculated using Equation 5 for $\rho = 10^{-9}$ m) were obtained for drops evaporating on microcavity surfaces. Figure 6 shows the magnitudes of P_γ , P_f and P_{eff} for FDLC-coated and PTFE-coated P6 microcavity surfaces. As described in Equation 7, when the effect of gravity is neglected, the effective pressure, P_{eff} , is the sum of the pressure due to the evaporation-induced flow (P_f) and the Laplace pressure (P_γ). At the end of the evaporation process, P_f increases rapidly, measuring more than an order of magnitude larger than P_γ . Hence, P_{eff} is completely dependent on P_f . This is the region where all the 1D wetting transitions (Figure 6(a)) were observed. In the cases where a 1D transition occurred, the P_{eff} values estimated at the time of the 1D transition were comparable to the wetting pressures of the corresponding surfaces (Figure 6(a)). For water droplet evaporation without a wetting transition, the P_{eff} at the end of the evaporation process was smaller than the threshold wetting pressure (Figure 6(b)). The threshold wetting pressure for the nontransition case was much higher than that of the 1D wetting transition case due to the small size of the microcavities and low surface energy of the coating.

A plot of the contact angle (θ) vs. the curvature radius (R) for various values of the drop base radius (r) is shown in Figure 7. For visualization purposes, the plot is divided into four regions based on the magnitude of P_f (obtained using Equation 5) for the corresponding drop parameters. It can be seen that P_f increases with increasing R , increasing r , and decreasing θ . The plot shows that P_f is comparable to P_γ (~ 200 Pa) for θ values as large as 40° with a drop radius of $750 \mu\text{m}$. P_f values are greater than $3,000$ Pa for contact angles as large as 15° and 25° with a base radius of $50 \mu\text{m}$ and $750 \mu\text{m}$, respectively. Further, to estimate P_f values on arbitrary substrates, experimental data for the drop parameters of a 1D transition were superimposed on the above plot. Most of the experimental data were located in region 3 and region 4, where the P_f values are greater than $1,000$ Pa and $3,000$ Pa, respectively. Few of the data points fell in the higher end of region 2, where P_f is $\sim 1,000$ Pa.

Figure 7 is useful for qualitatively estimating the wetting states by experimental drop shape parameters. However, it is noted that, we have used apparent contact angle values obtained from side-view measurements for estimation of pressure values shown in Figures 6 and 7. However, in reality, contact angle near to the three-phase contact line tends to accommodate to the local wettability. For a drop on the patterned surfaces, the severity of this deviation from the bulk behavior is shown to be related to the a/r_t ratio of the drop [32]. For a drop with $a/r_t > 0.06$, the contact angle tends to be dominantly influenced by local physicochemical factors. Most of the surfaces used in the study exhibited 1-D transitions when $a/r_t \sim 0.04$ to 0.2 . In such cases, the internal flow and pressure distribution near to the contact line may be different from that predicted using side-view measurements (Figures 6 and 7). Furthermore, role of surface patterning on the pressure and velocity distributions of the flow in the drop needs to be carefully considered. Hence, for quantitative prediction of 1D transition, improvement to drop measurement techniques and drop internal flow models is desirable.

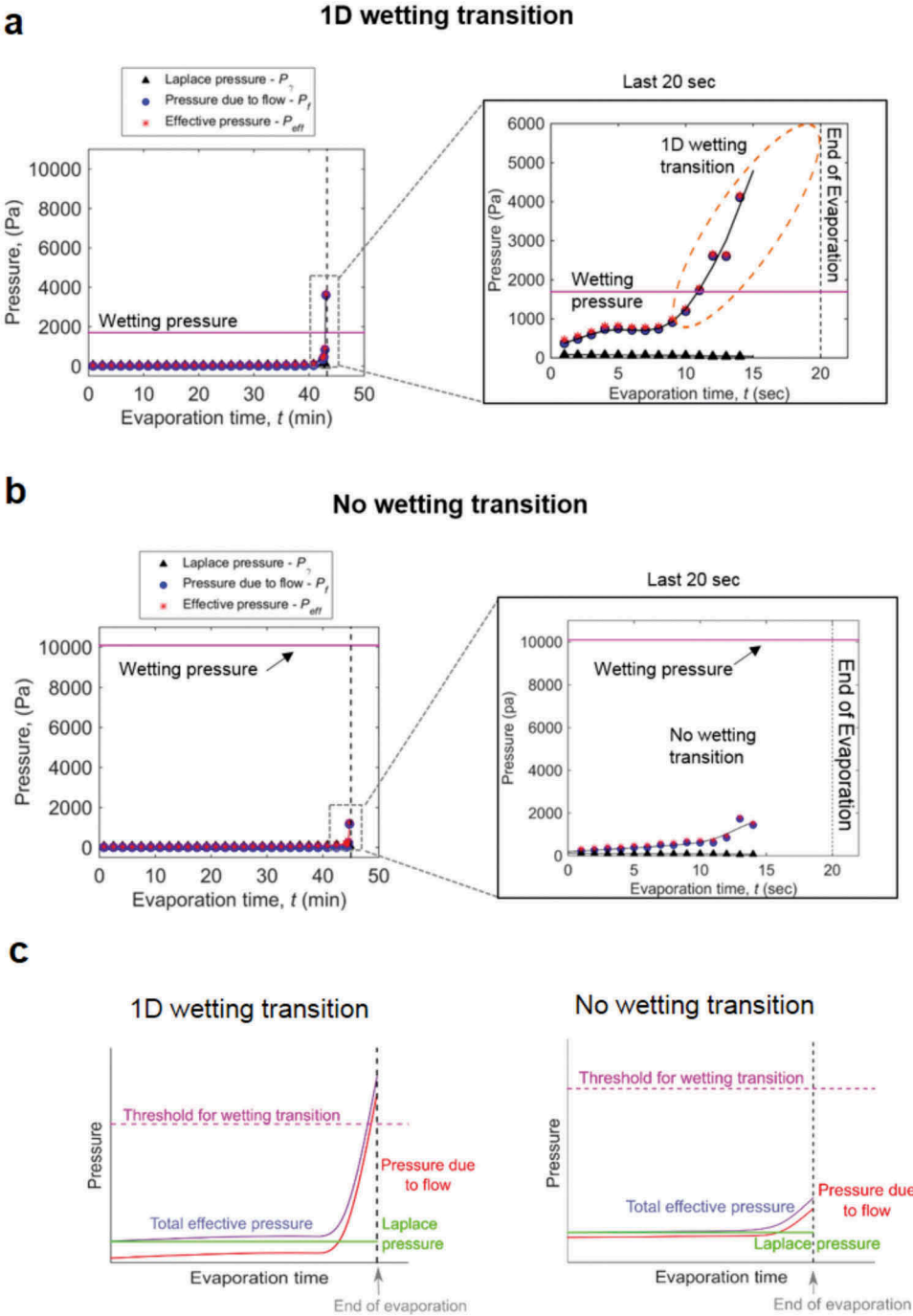


Figure 6. The flow pressure (P_f) at a microcavity as a determinant of an evaporation-induced wetting transition. The total pressure (P_{eff}) is the sum of the Laplace pressure (P_γ) and the pressure due to evaporation-induced flow (P_f). (a) Pressure characteristics on the FDLC-coated P6 surface. (b) Pressure characteristics on the PTFE-coated P6 surface. (c) Schematics detailing the pressure characteristics during evaporation for surfaces exhibiting a 1D wetting transition and for those not exhibiting wetting transitions. For the case of a drop exhibiting a 1D wetting transition, the total pressure exceeds the threshold of the wetting transition before complete evaporation of a droplet, thereby exhibiting a wetting transition. For the drop not exhibiting a wetting transition, although the evaporation-induced flow increases, the total pressure is low relative to the threshold pressure required for the wetting transition. Therefore, the wetting transition does not happen upon the evaporation of the water droplet.

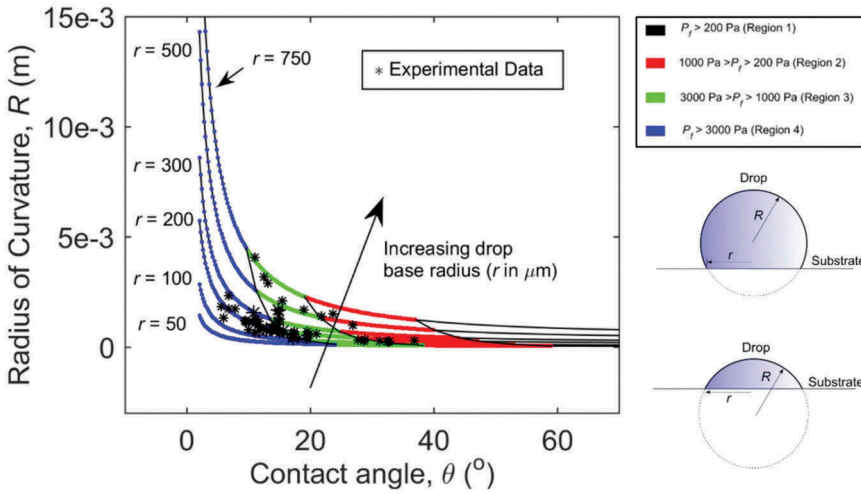


Figure 7. Plot of the contact angle vs. the curvature radius for various drop base radii. The plot is divided into four regions for visualization purposes according to the P_f values estimated using Equation 5 for the corresponding drop parameters. Experimental data show the parameters of the evaporating drop at the time point of the 1D transition on the experimental microcavity surfaces. Since the plot will help qualitatively estimate the effective pressures within a drop using only the drop shape parameters, it is useful for identifying the wetting states on a superhydrophobic surface with known wetting pressures.

Overall, the experimental and analytical results relate the mass transfer characteristics over the water droplet surface to the wetting characteristics at its base. This relationship will help the future design of processes for controlled deposition and transport of materials through differential mass transfer via evaporation on patterned and flat superhydrophobic surfaces. Furthermore, we envision that understanding of the characteristics of the 1D wetting transition *via* evaporation-mediated internal flow can be utilized in various applications, such as lab-on-a-chip technology, by altering the surface geometry, surface chemistry, drop geometry, and drop evaporation conditions. In addition, nonwetting superhydrophobic surfaces designed for engineering applications have wetting pressures higher than the typically expected Laplace pressures. Our results showed that the design of such surfaces should also consider the large pressures encountered when a drop is allowed to evaporate.

Conclusion

We demonstrated a new category of 1D Cassie-to-Wenzel wetting transitions based on the internal flow within a water droplet during evaporation. For this purpose, microscale cavity surfaces with a large range of wetting pressures (~ 250 Pa to 30,000 Pa) were generated by varying the cavity size and surface energy. The wetting transitions initially initiated near the contact line and then gradually progressed toward the center of the drop. The directional wetting transitions were observed on surfaces with wetting pressures of up to $\sim 7,568$ Pa. In situ evaporation experiments with a fluorescence microscope confirmed preferential depinning of the air-water interface in individual cavities near the three-phase contact line. We showed that the internal flow of the evaporating drop, which was previously neglected, controls the 1D wetting transition during evaporation. The estimated pressure due to the internal flow at the time point of the 1D wetting transition was high and comparable to the theoretical wetting pressure. Our results showed a direct relationship between the wetting characteristics of an evaporating drop and the nature of mass transfer during evaporation. This finding will help design differential mass transfer-based evaporative processes for controlled transport of small amounts of material on superhydrophobic, patterned surfaces.

Disclosure

The authors declare no conflict of interest.

Funding

This research was supported by the KIST Institutional Program (2E29200) and by the National Research Foundation of Korea (NRF) grant funded by the Korean Government (MSIT) (grant no. 2012R1A6A1029029, 2018R1A2A3075013, and 2019R1A2C2003407).

ORCID

Hong Nam Kim  <http://orcid.org/0000-0002-0329-0029>

Eui-Sung Yoon  <http://orcid.org/0000-0001-5804-6376>

References

- [1] B. D. Hatton and J. Aizenberg, "Writing on superhydrophobic nanopost arrays: Topographic design for bottom-up assembly," *Nano Lett.*, vol. 12, no. 9, pp.4551–4557, 2012. DOI: [10.1021/nl301775x](https://doi.org/10.1021/nl301775x).
- [2] R. Dufour, *et al.*, "Zipping effect on omniphobic surfaces for controlled deposition of minute amounts of fluid or colloids," *Small*, vol. 8, no. 8, pp. 1229–1236, 2012. DOI: [10.1002/sml.201101895](https://doi.org/10.1002/sml.201101895).
- [3] H. Mertaniemi, *et al.*, "Superhydrophobic tracks for low-friction, guided transport of water droplets," *Adv. Mater.*, vol. 23, no. 26, pp. 2911–2914, 2011. DOI: [10.1002/adma.201100461](https://doi.org/10.1002/adma.201100461).
- [4] J. W. Krumpfer and T. J. McCarthy, "Dip-coating crystallization on a superhydrophobic surface: A million mounted crystals in a 1 cm² array," *J. Am. Chem. Soc.*, vol. 133, no. 15, pp.5764–5766, 2011. DOI: [10.1021/ja2011548](https://doi.org/10.1021/ja2011548).
- [5] Y. Koc, *et al.*, "Nano-scale superhydrophobicity: Suppression of protein adsorption and promotion of flow-induced detachment," *Lab Chip*, vol. 8, no. 4, pp. 582–586, 2008. DOI: [10.1039/b716509a](https://doi.org/10.1039/b716509a).
- [6] M. R. Flynn and J. W. M. Bush, "Underwater breathing: The mechanics of plastron respiration," *J. Fluid Mech.*, vol. 608, pp. 275–296, 2008. DOI: [10.1017/S0022112008002048](https://doi.org/10.1017/S0022112008002048).
- [7] J. B. Boreyko and C.-H. Chen, "Self-propelled dropwise condensate on superhydrophobic surfaces," *Phys. Rev. Lett.*, vol. 103, no. 18, pp.184501, 2009. DOI: [10.1103/PhysRevLett.103.184501](https://doi.org/10.1103/PhysRevLett.103.184501).
- [8] N. Miljkovic, R. Enright, and E. N. Wang, "Effect of droplet morphology on growth dynamics and heat transfer during condensation on superhydrophobic nanostructured surfaces," *ACS Nano*, vol. 6, no. 2, pp.1776–1785, 2012. DOI: [10.1021/nn205052a](https://doi.org/10.1021/nn205052a).
- [9] N. Miljkovic and E. N. Wang, "Condensation heat transfer on superhydrophobic surfaces," *MRS Bull.*, vol. 38, no. 5, pp.397–406, 2013. DOI: [10.1557/mrs.2013.103](https://doi.org/10.1557/mrs.2013.103).
- [10] A. R. Betz, J. Jenkins, C.-J. C. Kim, and D. Attinger, "Boiling heat transfer on superhydrophilic, superhydrophobic, and superbiphilic surfaces," *Int. J. Heat Mass Transf.*, vol. 57, no. 2, pp.733–741, 2013. DOI: [10.1016/j.ijheatmasstransfer.2012.10.080](https://doi.org/10.1016/j.ijheatmasstransfer.2012.10.080).
- [11] N. A. Patankar, "Consolidation of hydrophobic transition criteria by using an approximate energy minimization approach," *Langmuir*, vol. 26, no. 11, pp.8941–8945, 2010. DOI: [10.1021/la9047424](https://doi.org/10.1021/la9047424).
- [12] A. Lafuma and D. Quere, "Superhydrophobic states," *Nat. Mater.*, vol. 2, no. 7, pp.457–460, 2003. DOI: [10.1038/nmat924](https://doi.org/10.1038/nmat924).
- [13] B. Liu and F. F. Lange, "Pressure induced transition between superhydrophobic states: Configuration diagrams and effect of surface feature size," *J. Colloid Interface Sci.*, vol. 298, no. 2, pp.899–909, 2006. DOI: [10.1016/j.jcis.2006.01.025](https://doi.org/10.1016/j.jcis.2006.01.025).
- [14] E. Bormashenko, *et al.*, "Characterization of rough surfaces with vibrated drops," *Phys. Chem. Chem. Phys.*, vol. 10, no. 27, pp. 4056–4061, 2008. DOI: [10.1039/b800091c](https://doi.org/10.1039/b800091c).
- [15] V. Bahadur and S. V. Garimella, "Preventing the cassie-wenzel transition using surfaces with noncommunicating roughness elements," *Langmuir*, vol. 25, no. 8, pp.4815–4820, 2009. DOI: [10.1021/la803691m](https://doi.org/10.1021/la803691m).
- [16] G. Whyman and E. Bormashenko, "Wetting transitions on rough substrates: General considerations," *J. Adhes. Sci. Technol.*, vol. 26, pp. 207–220, 2012.
- [17] M. S. Bobji, S. V. Kumar, A. Asthana, and R. N. Govardhan, "Underwater sustainability of the "cassie" state of wetting," *Langmuir*, vol. 25, no. 20, pp.12120–12126, 2009. DOI: [10.1021/la902679c](https://doi.org/10.1021/la902679c).
- [18] D. P. Maitland and A. Maitland, "Penetration of water into blind-ended capillary tubes and its bearing on the functional design of the lungs of soldier crabs *mictyris longicarpus*," *J. Exp. Biol.*, vol. 163, pp. 333, 1992.
- [19] P. Papadopoulos, L. Mammen, X. Deng, D. Vollmer, and H.-J. Butt, "How superhydrophobicity breaks down," *Proc. Natl. Acad. Sci.*, vol. 110, no. 9, pp.3254–3258, 2013. DOI: [10.1073/pnas.1218673110](https://doi.org/10.1073/pnas.1218673110).

- [20] M. Xu, G. Sun, and C.-J. Kim, “Infinite lifetime of underwater superhydrophobic states,” *Phys. Rev. Lett.*, vol. 113, no. 13, pp.136103, 2014. DOI: [10.1103/PhysRevLett.113.136103](https://doi.org/10.1103/PhysRevLett.113.136103).
- [21] Y. C. Jung and B. Bhushan, “Wetting transition of water droplets on superhydrophobic patterned surfaces,” *Scr. Mater.*, vol. 57, no. 12, pp.1057–1060, 2007. DOI: [10.1016/j.scriptamat.2007.09.004](https://doi.org/10.1016/j.scriptamat.2007.09.004).
- [22] E. Bormashenko, “Progress in understanding wetting transitions on rough surfaces,” *Adv. Colloid Interface Sci.*, vol. 222, pp. 92–103, 2015. DOI: [10.1016/j.cis.2014.02.009](https://doi.org/10.1016/j.cis.2014.02.009).
- [23] E. Bormashenko, R. Pogreb, G. Whyman, and M. Erlich, “Cassie–wenzel wetting transition in vibrating drops deposited on rough surfaces: Is the dynamic cassie–wenzel wetting transition a 2d or 1d affair?,” *Langmuir*, vol. 23, no. 12, pp.6501–6503, 2007. DOI: [10.1021/la700935x](https://doi.org/10.1021/la700935x).
- [24] E. Bormashenko, A. Musin, G. Whyman, and M. Zinigrad, “Wetting transitions and depinning of the triple line,” *Langmuir*, vol. 28, no. 7, pp.3460–3464, 2012. DOI: [10.1021/la204424n](https://doi.org/10.1021/la204424n).
- [25] C. U. Chan and C.-D. Ohl, “Total-internal-reflection-fluorescence microscopy for the study of nanobubble dynamics,” *Phys. Rev. Lett.*, vol. 109, no. 17, pp.174501, 2012. DOI: [10.1103/PhysRevLett.109.174501](https://doi.org/10.1103/PhysRevLett.109.174501).
- [26] X.-Y. Zheng, A. Harata, and T. Ogawa, “Study of the adsorptive behavior of water-soluble dye molecules (rhodamine 6g) at the air–water interface using confocal fluorescence microscope,” *Spectrochim. Acta, Part A*, vol. 57, no. 2, pp.315–322, 2001. DOI: [10.1016/S1386-1425\(00\)00389-9](https://doi.org/10.1016/S1386-1425(00)00389-9).
- [27] R. D. Deegan, *et al.*, “Capillary flow as the cause of ring stains from dried liquid drops,” *Nature*, vol. 389, no. 6653, pp. 827–829, 1997. DOI: [10.1038/39827](https://doi.org/10.1038/39827).
- [28] H. Gelderblom, O. Bloemen, and J. H. Snoeijer, “Stokes flow near the contact line of an evaporating drop,” *J. Fluid Mech.*, vol. 709, pp. 69–84, 2012. DOI: [10.1017/jfm.2012.321](https://doi.org/10.1017/jfm.2012.321).
- [29] Á. G. Marín, H. Gelderblom, D. Lohse, and J. H. Snoeijer, “Order-to-disorder transition in ring-shaped colloidal stains,” *Phys. Rev. Lett.*, vol. 107, no. 8, pp.085502, 2011. DOI: [10.1103/PhysRevLett.107.085502](https://doi.org/10.1103/PhysRevLett.107.085502).
- [30] G. Berteloot, C. T. Pham, A. Daerr, F. Lequeux, and L. Limat, “Evaporation-induced flow near a contact line: Consequences on coating and contact angle,” *Europhys. Lett.*, vol. 83, no. 1, pp.14003, 2008. DOI: [10.1209/0295-5075/83/14003](https://doi.org/10.1209/0295-5075/83/14003).
- [31] C. Huh and L. E. Scriven, “Hydrodynamic model of steady movement of a solid/liquid/fluid contact line,” *J. Colloid Interface Sci.*, vol. 35, no. 1, pp.85–101, 1971. DOI: [10.1016/0021-9797\(71\)90188-3](https://doi.org/10.1016/0021-9797(71)90188-3).
- [32] J. Carmeliet, L. Chen, Q. Kang, and D. Derome, “Beyond-cassie mode of wetting and local contact angles of droplets on checkboard-patterned surfaces,” *Langmuir*, vol. 33, no. 24, pp.6192–6200, 2017. DOI: [10.1021/acs.langmuir.7b01471](https://doi.org/10.1021/acs.langmuir.7b01471).